# Northumbria Research Link

Northumbria
University
NEWCASTLE

UniversityLibrary

# Ultra-thin N-doped carbon coated SnO₂ nanotubes as anode material for high performance lithium-ion batteries

Ziying Wen [a], Cuiping Gu [a, *], Yanjun Yin [b], Maryam Bayati [c], Terence Xiaoteng Liu [c, *], Jiarui Huang [a, *]

[a] Key Laboratory of Functional Molecular Solids, Ministry of Education, Anhui Provincial Engineering Laboratory for New-Energy Vehicle Battery Energy-Storage Materials, College of Chemistry and Materials Science, Anhui Normal University, Wuhu 241002, P.R. China

[b] School of Chemistry and Material Engineering, Chaohu University, Chaohu 238000, P.R. China

[c] Faculty of Engineering and Environment, Northumbria University, Newcastle upon Tyne NE1 8ST, U.K.

Corresponding authors:

J.R. Huang, email: jrhuang@ahnu.edu.cn

C.P. Gu, email: cpgu2008@ahnu.edu.cn

T.X. Liu, email: terence.liu@northumbria.ac.uk

**Abstract:** Tin dioxide nanotubes coated with ultrathin N-doped carbon film (N-doped SnO$_2$/C NTs) are prepared through a sacrificial template method for the first time. It was employed as anodes for lithium-ion batteries (LIBs) and delivered a high reversible capacity of 909.5 mAh g$^{-1}$ at 0.5 A g$^{-1}$ after 200 cycles, outstanding stability 551.7 mAh g$^{-1}$ after 500 cycles at 1 A g$^{-1}$, and excellent rate performance of 1069.2 mAh g$^{-1}$ after 280 cycles. Such superior electrochemical performance is owning to the N-doped carbon coating which improved the conductivity of the NTs, which is essential for higher performance LIBs. The special designed whole nanotube structure provides extensive surface and pores to accommodate Li, meanwhile, prohibited the volume expansion during cycling test. The electrochemical performance of pouch-type cells further demonstrates the SnO$_2$/C NTs as a promising candidate for LIBs anode. This study has shed a light on the LIB anode materials design and preparation and made such hollow nanostructured materials a potential candidate to replace commonly used graphite materials.

**Key words:** SnO$_2$; Nanotube; N-doped carbon coating; Lithium ion battery; Anode

## 1. Introduction

Lithium–ion batteries (LIBs) have become the dominant power source for electric/electronic devices and automobiles owning to their abundant reserves, memoryless effect, high capacity and environmental harmlessness [1, 2]. New materials research for each component within LIB has been conducted for purpose of improving their electrochemical performance in the past decades [3-5]. On the anode side, graphite is the most commonly used material. However, its theoretical capacity is not adequate for the current growing energy demand.[3] Therefore, alternative materials have been investigated to overcome this issue. For instance, Zheng et al. designed a yolk@shell $Fe_2O_3$@carbon anode exhibiting a high cyclic capacity of 1013 mAh g$^{-1}$ at 0.2 A g$^{-1}$ after 80 cycles [6]. Wang et al. synthesized $Co_3O_4$ nanotubes by template-free method which delivered a satisfied capacity of 1081.5 mAh g$^{-1}$ over 50 cycles at 0.1 A g$^{-1}$ [7]. Narsimulu et al. constructed $SnO_2$/carbon cloth nanocomposite via solvothermal process. The cell exhibited 1038 mAh g$^{-1}$ at 0.5 A g$^{-1}$ (50 cycles) as the capacity [8]. Among these materials, tin dioxide ($SnO_2$) stands out due to its outstanding theoretical capacity up to 1494 mA h g$^{-1}$ [9]. Further, as a promising anode material, $SnO_2$ shows other advantages over graphite in previous studies. Agostini et al. compared the lithium storage behavior between bulk graphite and exfoliated graphite/graphene nanosheets electrodes. According to the results, the performance of the latter was better, demonstrating that the single bulk structure is not conducive to the promotion of electrochemical performance [10]. Nevertheless, in past literature, numerous morphologies of $SnO_2$ have been designed, including nanoparticles [11-13],

nanospheres [14-16], nanofibers [17, 18], nanocubes [19-21], nanowires [22, 23], and so on, to tackle the structural problems and thus enhance their electrochemical capabilities. However, two main issues still hinder the development of $SnO_2$-based anode for LIBs, and strategies to enhance $SnO_2$-based anode performance for LIBs have been researched, methods generally lay into two aspects: (1) Drastic volume expansion (more than 300%) is associated with the process of lithiation/delithiation, which leads to the pulverization and shedding of $SnO_2$, resulting in rapid reversible capacity decay and reduced cycle performance [24]. This phenomenon requires fabrication of novel nanostructure which can withstand the impact to volume change during charge/discharge process, e.g. hollow nanostructured $SnO_2$ materials to maintain the stability to minimize the volume expansion [25]. (2) Poor conductivity of $SnO_2$ restricts the electrochemical kinetics, which leads to low rate capacity [13]. This can be overcame by adding conductive materials to improve its conductivity [26]. However, it is worth noting that the carbon content ratio plays an important role, and it has to be carefully controlled, otherwise it may cause agglomeration of $SnO_2$ when anchoring nano-sized $SnO_2$ particles to the carbon matrix, and lead to a decay of reversible capacity after long-time cycling. For instance, Fu *et al*. prepared $SnO_2$@C composites with $SnO_2$ nanocrystals anchored on carbon matrix which delivers weak rate performance when used as anode for LIBs [27]. Li *et al*. synthesized $SnO_2$/C composites in which ultrafine $SnO_2$ nanoparticles are bounded in 3D N-doped carbon cages as anode for LIBs, revealing well rapid charging/discharging capability, however, the capacity tends to decline fast during durability cycling test [28]. Moreover, it is

worth mentioning that the N–doped carbon matrix cannot only merely improve the electrical conductivity, but also restrain the agglomeration of $SnO_2$ during the reversible reaction [9, 11, 28].

Recently, it has been suggested that carbon coating on the surface of hollow $SnO_2$ nano structure can tolerant sufficient volume change expansion, and the results showed that the electrochemical performance of hollow structured $SnO_2/C$ composite electrodes had been obviously improved [17, 20, 29, 30]. However, the most common products of hollow structured nanosized $SnO_2$ are in spherical shape [31-33]. This is because the preparation methods that uses silica and polymer nanospheres as the template to maintain the deposition and growth of $SnO_2$ nanocrystals, but the subsequent process of template removal is complicated [14, 34-37].

Herein, we explored a facile strategy to synthesize the N-doped carbon coated porous $SnO_2$ nanotubes ($SnO_2/C$ NTs) through a facile co–precipitation hydrothermal treatment process. $CuSn(OH)_6$ nanorods as precursor was used in our previous work [38] this time, the precursor was partially etched by the acid and generated the hollow structure, which can improve the contact with the electrolyte and thus stabilizes the structure in the charge/discharge process. After calcination, we use polydopamine formed a graphitized N–doped carbon film uniformly coated on the surface of the nanotubes, which helps to improve the electrical conductivity and inhibit the volume change. The $SnO_2/C$ NTs coated with N-doped carbon is tested as the anode for LIB, and it exhibited excellent electrochemical performance with high capacity of 909.5 mAh g$^{-1}$ at 0.5 A g$^{-1}$ over 200 cycles, and durability with reversible capacity of

551.7 mA h g$^{-1}$ after 500 cycles at 1 A g$^{-1}$, owing to the outer N-doped carbon-coated can be used as a buffer layer to cope with the volume expansion of SnO$_2$ during cycles. Furthermore, it is become clear that the rate performance is stable after three rounds of repeated tests, indicating its high recovery rate, which is attributed to the improving electrical conductivity and sufficient internal cavity to accommodate the transport of lithium–ion.

## 2. Experimental section

2.1 Material synthesis

Chemical and reagents were used as received. Scheme 1 shows the preparation procedure of carbon coated SnO$_2$ nanotubes (SnO$_2$/C NTs), which is described in three steps below.

2.1.1 Synthesis of CuSn(OH)$_6$ nanorods

Briefly, 1.58 g of SnCl$_4$·5H$_2$O was dissolved in 180 mL of di-ionized (DI) water at temperature of 30°C, 1.52 g of NaOH was then added under vigorous stirring followed by adding 100 mL of CuCl$_2$·H$_2$O (0.044 M) solution then the mixture was stirred for 15 minutes, lead to formation of blue colour precipitate. The mixture was then kept at room temperature for 6 h. The resultant precipitate was then separated, washed, dried, and the CuSn(OH)$_6$ nanorods are obtained shown in Scheme. 1b.

2.1.2 Synthesis of SnO$_2$ NTs

0.1 g of the as prepared CuSn(OH)$_6$ nanorods was dispersed into 0.3 mL acetic acid (CH$_3$COOH) in 30 mL DI water under ultrasound mixing for 0.5 h, followed by transferring into a 50 mL Teflon-lined autoclave and kept at 180°C for 12 h, white

precipitate was then formed. After cooling down to room temperature, the yield was separated using centrifuge, and rinsed with deionized water and anhydrous ethanol for several times. The sample was dried at 60°C for 24 h, then $SnO_2$ nanotubes ($SnO_2$ NTs) was obtained and shown in Scheme. 1c. For comparison, the $SnO_2$ NTs were annealed at 600°C and 700°C for 2 h in air, and denoted as $SnO_2$-600 NTs and $SnO_2$-700 NTs, respectively. In addition, porous $SnO_2$ nanorods ($SnO_2$ NRs) were also prepared by a chemical solution route followed by calcination and acid-washing process according to our previous work [38].

2.1.3 Synthesis of $SnO_2$/C NTs

To prepare the $SnO_2$/C NTs, 0.2 g of as-obtained $SnO_2$ NTs was mixed with 60 mg dopamine hydrochloride ($C_8H_{11}NO_2 \cdot HCl$) in Tris–buffer (50 mL, 10 mM) at pH 8.5 for 24 h. The sample was collected using the same method to $SnO_2$ NTs, and then carbonized under $N_2$ atmosphere at 500°C for 4 h to obtain $SnO_2$/C NTs and shown in Scheme. 1d. The $SnO_2$/C NRs were obtained through the same carbon coating process. For comparison, the $SnO_2$/C NTs composites reacted with 20 mg and 80 mg dopamine hydrochloride were conducted and denoted as $SnO_2$/C–20 NTs and $SnO_2$/C–80 NTs, respectively.

**3. Results and discussion**

The $SnO_2$/C NTs composite was produced using three steps as shown in Scheme 1. The preparation process of $SnO_2$ NTs mainly involves the following equations:

$$SnCl_4 + 6NaOH + CuCl_2 \rightarrow CuSn(OH)_6 \downarrow + 6NaCl \qquad (Eq. 1)$$

$$CuSn(OH)_6 + 2CH_3COOH \rightarrow Cu(CH_3COO)_2 + SnO_2 + 4H_2O \qquad (Eq. 2)$$

First, rod-like $CuSn(OH)_6$ precursor was derived from an aqueous solution process through equation (1). In the co-precipitation process, $SnCl_4$ reacted with excess NaOH to produce $Na_2SnO_3$ firstly, and then $CuCl_2$ solution was added to the above solution, resulting in $CuSn(OH)_6$ nucleus. In order to reduce the energy of the system, some of nucleus aggregated together. In the latter crystal growth process, some new nucleus kept forming and aggregated together. The as-formed nucleus are of hexagonal nature and these hexagonal nucleus aggregate to form rod-like $CuSn(OH)_6$. Second, the rod-like $CuSn(OH)_6$ precursor reacted with acetic acid under hydrothermal condition according to equation (2). Because this reaction is a heterogeneous reaction, and the above chemical reactions mainly occurred on the surface of $CuSn(OH)_6$ rods. When the surface of $CuSn(OH)_6$ rods has converted to insoluble $SnO_2$ and soluble $Cu(CH_3COO)_2$, the internal substances of $CuSn(OH)_6$ rods diffuse to the outer surface and continue to react with acetic acid, resulting in $SnO_2$ NTs. Therefore, the rod-like $CuSn(OH)_6$ precursor served as sacrificial template in the preparation process of $SnO_2$ NTs. Finally, the surface of $SnO_2$ NTs was covered by polydopamine (PDA) followed by a carbonization process, yielding the $SnO_2/C$ NTs.

SEM and TEM images of $CuSn(OH)_6$ in Fig. 1a and 1d indicate hexagonal $CuSn(OH)_6$ nanorods have size of ~1 μm in length and ~210 nm in side length. Fig. 1b and 1e show the surface of the as-prepared $SnO_2$ NTs with size of ~1.1 μm in length, 350 nm in outside diameter and 180 nm in internal diameter prepared using hydrothermal reaction, it can be seen that the surface of the NTs are rough and the length has hardly decreased. The solid structure has also transformed into hollow $SnO_2$ NTs.

EDS elemental analysis (Fig. S1b) revealed that only Sn and O elements present in the product, this is the evidence that any impurities have been removed for next preparation step. After constant stirring in polymerize dopamine followed by carbonization, the SnO$_2$/C NTs were obtained with good integrity in size and tubular structure (Fig. 1c and 1 f). Further observation of high magnification TEM images (Fig. 1g) displayed that the SnO$_2$/C NT was composed of nanocrystals and wrapped in ultrathin carbon layer (the light areas at the edges), which improves the conductivity of pure SnO$_2$ greatly. To take a deeper look at the edge of the region, as performed by high-resolution TEM (HRTEM) in Fig. 1h, identifying the outer carbon layer was amorphous with thickness of ~5 nm, and the well-defined lattice fringe spacing of 0.335 nm are assigned to the (110) plane of SnO$_2$. Meanwhile, the selected area electron diffraction (SAED) pattern (Fig. 1i) has definitely shown the diffraction patterns of SnO$_2$. The bright diffraction rings (110), (101), (211), and (112) confirm the good crystallinity of SnO$_2$/C NTs. Upon comparison of Fig. 1a-c, the as-prepared SnO$_2$ NRs (Figs. S2a, b) have similar particle size and non-hollow porous structure. After carbon coating, the pores on the surface of SnO$_2$/C NRs shown in Figs. S2c, d become small and their surface turns to smooth due to the carbon coating. As for the SEM images of SnO$_2$-600 NTs and SnO$_2$-700 NTs shown in Figs. S2e-h, SnO$_2$-700 NTs exhibit obviously porous structure on the surface of nanotubes because of the high calcination temperature. After carbon coating, the surface of SnO$_2$-600/C NTs and SnO$_2$-700/C NTs shown in Figs. S2i-l also become smooth. Moreover, the SEM images of SnO$_2$/C–20 NTs and SnO$_2$/C–80 NTs are shown in Figs. S2m-p. It can be seen that the surface of SnO$_2$/C–80 NTs becomes very smooth

9

Fig 2a. exhibits the XRD patterns of as prepared $SnO_2$ NTs and $SnO_2$/C NTs. All diffraction peaks are matched with the rutile phase $SnO_2$ (JCPDS card No. 45-1445). However, in $SnO_2$/C NTs, there is no diffraction peaks corresponding to carbon are found owning to the amorphous structured caused by low carbonization temperature. This result is in consistence with Fig 1h. Fig. 2b exhibits the Raman spectrum of $SnO_2$/C NTs. The two broad peaks located at 1364 and 1584 $cm^{-1}$ are corresponding to disordered structure (D band) and graphite structure (G band) of carbon, respectively [39]. Moreover, it can be further divided into four peaks, which are located at 1214, 1366, 1527, and 1598 $cm^{-1}$. Among them, the peaks at 1598 and 1366 $cm^{-1}$ are attributed to the $sp^2$ hybrid carbon atoms, and the other at 1527 and 1214 $cm^{-1}$ are attributed to $sp^3$ hybrid carbons. After calculation, the ratio of $sp^2/sp^3$ for $SnO_2$/C NTs was 1.26, indicating that amorphous carbon layer has good conductivity after carbonization, which can rapidly transfer electrons for $SnO_2$ in the process of charge/discharge, thereby enhancing the rate performance effectively [29].

To confirm the carbon content of $SnO_2$/C NT composites, thermogravimetric analysis (TGA) results were carried out from 0 to 600ºC under air. As shown in Fig. 2c, there are two stage of weight loss for samples. Initially, the weight loss before 200ºC can be assigned to the release of adsorbed oxygen and water adsorbed on surface [40]. Subsequently, a second weight loss observed around 200–600ºC, reflecting the oxidation reaction of carbon layer on $SnO_2$/C, and the contents of carbon-coated

approximately accounts for 12.9%. From the TGA curves of the $SnO_2/C$–20 NTs and $SnO_2/C$–80 NTs shown in Figs. S3a, b, the contents of carbon are estimated as 6.7% and 18.2%, respectively. Fig. 2d shows the $N_2$ adsorption/desorption isotherms of $SnO_2/C$ NTs, the curves reveal the characteristics of type IV with an H1 type hysteresis loop. Moreover, the pore size distribution curve is presented in Fig. 2d (inset) accordingly, the major distribution of micro- and meso-pores are mainly attributed to the porous carbon layer after calcination and the reassembly of $SnO_2$ particles in the hydrothermal reaction. As a comparison, the $N_2$ adsorption/desorption isotherms of pure $SnO_2$ NTs and some other $SnO_2$-based materials under the same test conditions are shown in Figs. S3c-g. Additionally, the BET surface area and relevant information of pore size for the $SnO_2$-based materials are summarized in Table S1. The specific surface area of $SnO_2$ NTs and $SnO_2/C$ NTs are calculated as 128.3 and 92.9 $m^2\,g^{-1}$, respectively, which effectively promote the contact with electrolyte and buffer volume expansion of $SnO_2$ particles in charge/discharge process. Compared with the pore size distribution curve of the $SnO_2$ NTs, the pore volume and average pore size of the $SnO_2/C$ NTs decrease as listed in Table S1 for detail. Similar phenomenon is found in previous work [41]. Moreover, the carbon coating layer can closely attach on the surface of $SnO_2$ nanocreastals, which is confirmed by HRTEM image of the $SnO_2/C$ NTs shown in Fig. 1h. Therefore, partial pores could be occupied by carbon produced by carbonizing polydopamine, resulting in a reduction of specific surface area after carbon-coating, which could save the loss of electrolyte due to surface electrochemical reactions. The XPS results of two samples were exhibited in Figs. 2e–h and Figs. S3h–l. In Fig. 2e,

the presence of Sn, O, C, N were marked in the survey spectrum of the prepared $SnO_2$/C NTs. The Sn 3d spectrum is fitted into Sn $3d_{5/2}$(487.2 eV) and Sn $3d_{3/2}$(495.6 eV), respectively (Fig. 2f) [11, 42]. O 1s peaks at 530.9, 531.5, 532.4 eV are assigned to Sn–O, Sn–O–C, and C=O, respectively (Fig. 2g) [29, 43]. In the C 1s spectrum (Fig. 2h), four peaks correspond to C–C bond (284.8 eV), C–N/C=N bond (285.6 eV), C–O bond (286.4 eV), and the C=O bond (288.6 eV) [11, 26]. Additionally, the N 1s high-resolution spectrum was divided into three peaks located at 401.3, 400.5 and 398.8 eV, which are associated with graphitic N, pyrrolic N, and pyridinic N, respectively (Fig. S2b) [44-46]. In a word, Figs. 2e–h and Fig. S3h verified the successful formation of dopamine–derived N–doped carbon layer coated on the outer $SnO_2$ NTs. The XPS results of $SnO_2$ NTs shown in Figs. S3i–l indicate that the product is pure $SnO_2$ without any other impurity.

The $SnO_2$/C NTs were assembled in LIBs as anode and the electrochemical performance was analyzed using galvanostatic discharge/charge test, CV test and impedance test. Pure $SnO_2$ NT anode was also studied as comparison. As displayed in Fig. 3a, the enhanced rate performance of $SnO_2$/C NTs was measured at 0.1, 0.2, 0.5, 1, 2, and 5 A $g^{-1}$ for three times, corresponding to the first round of the discharge capacities of 1010.1, 829.4, 759.2, 681.0, 566.4, and 318.6 mA h $g^{-1}$, respectively. After that, it still showed a prominent reversible capacity of 1069.2 mA h $g^{-1}$ after 280 cycles, when the current density returned to 0.1 A $g^{-1}$, revealing the outstanding rate capability. Furthermore, the rate performance for pure $SnO_2$ NT electrode was conducted under the same test conditions, the capacities can maintain 1436.9, 628.9, 458.2, 346.5, 238.2,

and 111.5 mA h g$^{-1}$, respectively. However, when it was recovered to 0.1 A g$^{-1}$ for testing, the capacity can be returned to only 758.6 mA h g$^{-1}$ after 280 cycles. By comparison, pure SnO$_2$ NT electrode has poorer reversible capacity can be observed easily. However, the capacity increased at low current densities after cycling at different current densities, probably due to the gradual sufficient contact of the porous material with electrolyte and the ultra-small nanocrystals of refined SnO$_2$. Besides, the increasing trend of SnO$_2$ NTs is more obvious for this phenomenon, indicating that N–doped could supply further active sites in terms of extra interfacial Li$^+$ storage [11, 43]. The galvanostatic charge/discharge curves of two samples at different current densities were displayed in Fig. 3b and Fig. S4a, corresponding to the rate performance of Fig. 3a, respectively. To further demonstrate the excellent rate performance of the SnO$_2$/C NT electrode, it was tested at very high current densities of 8.0 and 12.0 A g$^{-1}$. The result shown in Fig. S4b demonstrates that the SnO$_2$/C NT electrode maintains high capacities even at the high current densities (8.0 A g$^{-1}$: 257.8 mA h g$^{-1}$, 12.0 A g$^{-1}$: 116.7 mA h g$^{-1}$). Moreover, when the current density recovered to 0.1 A g$^{-1}$, the capacity returned to a high value of 1030.5 mA h g$^{-1}$, demonstrating its prominent rate performance. To investigate the influence of hollow structure on the electrochemical performances of SnO$_2$/C NT anode, the rate performances of porous SnO$_2$ NR and porous SnO$_2$/C NR electrodes were tested and shown in Fig. S4c. Compared with the porous SnO$_2$ NR and porous SnO$_2$/C NR anodes, the SnO$_2$ NT and SnO$_2$/C NT anodes exhibited higher capacities at various current densities, indicating that the hollow structure could obviously improve their rate performance. The comparison of cyclic

process of $SnO_2$/C NTs electrode and pure $SnO_2$ NT electrode at 0.5 and 1 A g$^{-1}$ are plotted in Fig. 3c and Fig. 3d. Fig. 3c presents the cycling performance at 0.5 A g$^{-1}$ for 200 cycles. The initial cycle of $SnO_2$/C NT electrode exhibits a satisfactory discharge capacity of 1270.5 mA h g$^{-1}$, and charge capacity of 896.9 mAh g$^{-1}$. In addition, the specific capacity of $SnO_2$/C NTs was 909.5 mA h g$^{-1}$ after 200 cycles, which was much better than that of pure $SnO_2$ NTs (492.7 mAh g$^{-1}$), exhibiting higher electrochemical cyclic stability. Additionally, the initial Coulombic efficiency (ICE) of the $SnO_2$/C NT electrode was 70.6%, wherein the irreversible loss of capacity was ascribed to form SEI layer after electrolyte decomposition. The ICE of $SnO_2$/C NT electrode is well below 80%, which hampers its application in full-cell assembly. This is due to the high exposed surface of the as-prepared $SnO_2$ NTs, and the formation of SEI layer on the surface leads to a large irreversible initial capacity loss [47]. Therefore, reducing the specific surface area of $SnO_2$ anode material may enhance the ICE of the $SnO_2$ electrode. On the other hand, the large specific surface area of anode material can reduce the transport way of Li ions and buffer the volume expansion during the Li$^+$ insertion and extraction process, thus enhancing LIBs rate/cycling performance. Therefore, the rate/cycling performance of the $SnO_2$ anode would be decreased when the specific surface area of $SnO_2$ anode material was reduced. To overcome its shortage in the low ICE, the $SnO_2$/C can be controllably prelithiated by the lithium-biphenyl reagent [47, 48]. However, at the third cycle, the ICE increased rapidly to 95.3%, demonstrating that the irreversible process only had an impact on the initial cycles. The relatively high ICE of $SnO_2$/C is mainly due to the carbon layer coating on $SnO_2$.

Because it can effectively protect $SnO_2$ from contacting the electrolyte directly, thus reducing the electrolyte decomposition and inhibiting the formation of SEI layer. Moreover, to further elaborate the effect of reversible lithium-ion transport, the capacities in the potential range of 0.01~1.0 V (dealloying reaction) and 1.0~3.0 V (conversion reaction) were divided as a function of cycle number. The capacity contribution of $Sn/Li_2O$ to $SnO_2$ reaction at 1.0 V to 3.0 V is much higher than that of the dealloying reaction of $Li_xSn$ in Fig. S4d. Besides, at 0.01~1.0 V, the reversible capacity contribution of $Li_xSn$ dealloying reaction remains almost unchanged, while the contribution of $SnO_2$ reformation capacity increased slightly in the subsequent cycle, which was consistent with the change of total capacity during the cycle. The above results indicate that the increase of the capacity of $SnO_2$/C NT electrode at 0.5 A g$^{-1}$ for 200 cycles is mostly owe to the enhancement of conversion reaction efficiency in the voltage at 1.0~3.0 V [43]. Moreover, the voltage-capacity contribution curves of pure $SnO_2$ NT electrode under the same conditions are also shown in Fig. S4e. The bar chart reveals the capacity of dealloying reaction decreases gradually, while the contribution of reversible capacity of $SnO_2$ reformation decreases first and then increases (consistent with the cycle curve). It is shown that the solid electrolyte interface (SEI) film has a certain influence on the initial reversible capacity of pure $SnO_2$ NT electrode, but the $SnO_2$ still has a certain regenerative capacity during the cycling process. This is a further illustration that the carbon-coating process not only has a great promoting effect on the lithium-ion transport, but also improves decrease of the initial capacity during the cycle of prepared tubular $SnO_2$ electrode. For comparison, the cycling performances

the porous $SnO_2$ NR and porous $SnO_2$/C NR electrodes at 0.5 A g$^{-1}$ were tested and shown in Fig. S4f. It can be found that the porous $SnO_2$ NR anode exhibits a lower capacity than that of $SnO_2$ NT anode after 100 cycles. And the porous $SnO_2$/C NR anode also exhibits a lower capacity than that of $SnO_2$/C NT anode after 100 cycles. These results indicate that hollow structure can reduce the volume expansion of $SnO_2$ during cycling process, resulting in high cycling performance. To get a deep investigation into the excellent long-term cyclic stability of two anodes, another cycling performance at 1.0 A g$^{-1}$ was measured (first ten cycles at 0.1 and 0.5 A g$^{-1}$ for activation) in Fig. 3d. Unsurprisingly, throughout 500 cycles, the $SnO_2$/C NT electrode exhibited a prominent capacity of 551.7 mA h g$^{-1}$, which was higher than that of pure $SnO_2$ NT electrode (339.7 mA h g$^{-1}$). In addition, long-term cycling stability of $SnO_2$/C NT anode at a high current density of 2.0 A g$^{-1}$ was also tested and shown in Fig. S4g. The $SnO_2$/C NT anode delivered a high capacity of 340.5 mA h g$^{-1}$ even after 1000 cycles. Furthermore, cycling tests at diverse charge/discharge rates are measured as well. As shown in Fig. S4h, the capacities at charge/discharge rates of 0.4/0.6 A g$^{-1}$ were maintained at 655.4 and 458.9 mA h g$^{-1}$ for two electrodes, respectively. Moreover, even at the changeable charge/discharge rates, the electrodes still exhibited the reversible capacities of 930.3 and 858.2 mA h g$^{-1}$ (Fig. S4i), indicating that they have a great application prospect. Therefore, for $SnO_2$ NT electrode as anode of LIBs, it could be demonstrated that N-doped carbon film has a positive effect on the electrochemical performance, especially in the aspects of specific capacity and cyclic stability.

To investigate the influence of specific surface area and pore sizes on the

16

electrochemical performance, the rate/cycling performances of $SnO_2$-600 NT, $SnO_2$-600/C NT, $SnO_2$-700 NT and $SnO_2$-700/C NT electrodes were also studied. From Figs. S5a, b, it can be found that the $SnO_2$-600 NTs with large specific surface area and high pore volume exhibit higher rate/cycling performance than that of $SnO_2$-700 NTs. As for the rate/cycling performances of $SnO_2$-600/C NT and $SnO_2$-700/C NT electrodes shown in Figs. S5c, d, similar results can be founded. Because the $SnO_2$-600 NTs and $SnO_2$-600/C NT have large specific surface area and high pore volume, which can reduce the transport way of Li ions and buffer the volume expansion during the $Li^+$ insertion and extraction process [49]. Therefore, the $SnO_2$/C NTs with the largest specific surface area and the highest pore volume among these $SnO_2$/C composites exhibit the best rate/cycling performance.

To further investigate the influence of carbon coating content on the electrochemical performance of $SnO_2$/C NT anode, the rate/cycling performance of $SnO_2$/C–20 NT and $SnO_2$/C–80 NT electrodes were tested and shown in Fig. S6. From Fig. S6a, it can be found that $SnO_2$/C–20 NTs cycled at 0.5 A $g^{-1}$ delivers a higher capacity than that of $SnO_2$/C–80 NTs after 130 cycles. Furthermore, as shown in Fig. S6b, the $SnO_2$/C–20 NTs also exhibit superior cycling performance than that of $SnO_2$/C–80 NTs especially at the high current densities. This is mainly because tin dioxide has a higher theoretical specific capacity than that of carbon. Furthermore, the $SnO_2$/C–20 NTs have larger specific surface area and higher pore volume than those of $SnO_2$/C–80 NTs, which can reduce the transport way of Li ions and buffer the volume expansion during the $Li^+$ insertion and extraction process, resulting in the high

17

Figs. 4a, b shows the initial five CV curves of SnO$_2$/C NTs and pure SnO$_2$ NTs at a scan rate of 0.1 mV s$^{-1}$. In Fig. 4a, based on the reported literature [19, 50-52], the broad peak (1) at 0.83 V in first discharge scan can be related with the reduction of SnO$_2$ to metallic Sn (SnO$_2$ + 4Li$^+$ +4e$^-$ ↔ Sn + 2Li$_2$O), with the generation of Li$_2$O and irreversible SEI film. Then, the cathodic peak turns sharp, located at a voltage about 0.08 V (peak 2), which was corresponded to the reversible reaction of Li-Sn alloying (Sn + $x$Li$^+$ + $x$e$^-$ ↔ Li$x$Sn). Moreover, during the first anodic scan, the peak (3) at 0.56 V featured the dealloying reaction of Li$x$Sn alloys. The broad peak (4) at 1.24 V shows the reversible oxidation reaction of Sn/ Li$_2$O to SnO$_2$. Further, the peaks above do not overlap completely after the first scanning. The peak (1) shifts to the right (about 1.14 V) in the following four cycles, which may account for the partial reversible reaction of SnO$_2$ and Li$^+$ [53]. The peak (2) is divided into two small peaks, among which the small peak on the left can be ascribed to the intercalation of Li$^+$ on the carbon layer(C + $x$Li$^+$ + $x$e$^-$ →Li$x$C) [28]. Additionally, the other small peak shifts to higher voltages with peak area decreases, which was related to the loss of capacity caused by the irreversible side reactions after the first circle [19]. Moreover, the CV curves of the two electrodes during following four cycles are well overlapped, demonstrating the good electrochemical reversibility after the first cycle in SnO$_2$/C NT and pure SnO$_2$ electrode. Significantly, compared with the SnO$_2$ NT electrode (Fig. 4b), the redox peaks of SnO$_2$/C are more obvious, which indicates that carbon film can improve the reversibility of electrochemical reactions during lithiation/delithiation process. Figs. 4c,

d exhibited the galvanostatic charge/discharge curves of two electrodes at 0.5 A g$^{-1}$ for 200 cycles (as mentioned in Fig. 3c above). Clearly, the plateaus of these curves are basically consistent with the CV results above. Moreover, the selected curves of SnO$_2$/C NTs in Fig. 4c exhibit slight changes, but the overlap of pure SnO$_2$ NTs under the same conditions (Fig. 4d) is only in the first three cycles and in the 100th and 200th cycles, respectively, which indicates the SnO$_2$/C NT electrode has higher favorable reversible lithium storage capacity than that of SnO$_2$ NT electrode. For further compare the electrochemical reaction between SnO$_2$/C NT and pure SnO$_2$ electrodes, the differential charge capacity plots (DCPs) are exhibited (Figs. 4e, f). The peaks located at ca. 0.76 and 0.56 V, are correlated with the redox peaks marked on the CV curves, representing the generation of Li$_2$O, and the decomposition of Li$x$Sn, respectively. Moreover, the peaks on the CV curves of SnO$_2$/C NT electrode are sharper than those in pure SnO$_2$ NTs, indicating the faster reaction kinetics and superior electrode reversibility in LIBs.

In order to assess the rate behavior between SnO$_2$/C NT and pure SnO$_2$ NT electrodes, the capacitive characteristics for energy storage have been studied. Firstly, the CV curves have been measured in Figs. 5a, b. As scan rates increased, the absolute values of peak currents have increased gradually. The dominant mechanism between the surface-controlled process (SCP) and diffusion-controlled process (DCP) can be identified on the basis of the relation: $i = k_1 v^{1/2} + k_2 v = a v^b$, where $i$ and $v$ denote the peak currents and scan rate, respectively, $a$ and $b$ are adjustable parameters, $k_1 v^{1/2}$ is the DCP mechanism, and $k_2 v$ represent SCP mechanism [54]. When the $b$-value is approximate 0.5, the lithium storage behavior is dominated by DCP. While it is

approach 1.0, indicating that SCP makes the most contribution to the electrochemical reaction [43]. By linear fitting of $\log(i)$ and $\log(v)$, the $b$-values under different peak currents are obtained in Fig. 5c, d. The two pairs of sharpest oxidation and reduction peak $b$-values for $SnO_2$/C NT and $SnO_2$ NT electrodes are respectively fitted to be 0.82/0.78 and 0.75/0.65. Therefore, it can be inferred that the SCP dominated the high capacitance contribution, thus promoting the reaction kinetics. Moreover, the $b$–values are nearer to 1 (the reduction peaks), indicating the lithiation process in redox process is more rapid than delithiation process. It is noteworthy that the $b$–values of $SnO_2$/C NT electrode are slightly higher than those of the pure $SnO_2$ NTs, which demonstrates that the carbon layer has improved the surface electrochemical kinetics without destroying the original lithium storage mechanism of pure $SnO_2$ NTs. In addition, the calculated SCP contribution of redox reaction for two electrodes at different scan rates has been displayed in Figs. 5e, f (blue region). It can be observed that the SCP contribution always dominate and increases gradually with the increase of sweep rates. Specifically, the unique tubular structure, N–doped carbon matrix and uniform carbon-coated layer contribute to the higher capacitance contribution for $SnO_2$/C NT electrode, which indicates that it can support rapid electron transfer and demonstrate superior electrochemical performance.

To demonstrate the relationship between cyclic performance and electrode kinetics of $SnO_2$/C NTs, galvanostatic cyclability was performed at a 0.1 A $g^{-1}$ for 350 cycles and the result was shown in Fig. S7a. The electrochemical impedance spectroscopy (EIS) was performed and shown in Fig. 6a. It's not hard to see that with the increase of

cycle numbers, the reversible capacity was first increased and then decreased. Correspondingly, to explain this phenomenon, Nyquist plots of fresh cells, cells after 250 cycles, and cells after 350 cycles were obtained from the $SnO_2/C$ NT electrode. In Fig. 6a, each Nyquist plot contains a semicircle in the high–frequency region, representing the transfer resistance of the migration within the SEI layer for lithium-ion ($R_2$). A depressed semicircle in the medium-frequency is associated with the electron transport resistance of electrons ($R_{ct}$), and sloped line to the real axis in the low–frequency region, which related to the diffusion process of lithium-ion, representing the resistance of Warburg impedance ($Z_w$) [12]. The above circuit parameters are shown in the equivalent circuit (Fig. 6b), which fits the EIS spectrum in Fig. 6a well. In this, $R_1$ is assigned to the internal resistance among the composite and collector, and is the intercept of the semicircle on the Z' -axis at high–frequency. The fitting parameters of $R_1$, $R_2$, and $R_{ct}$ are displayed in Table S2. It is obvious that, the values of $R_{ct}$ of $SnO_2/C$ electrode after 250 cycles was 6.1 Ω, far less than the 69.1 Ω of the fresh cell and 69.7 Ω after 350 cycles, indicating that the electron transfer rate increases first and then decreases, which are consistent with the cycle performance (Fig. S7a). Significantly, the values of $R_{ct}$ (250 cycles) decreases sharply because of the formation of ultrafine nanocrystals from $SnO_2$ nanoparticles. Moreover, the fitting value of $R_1$ of fresh cell was about 6.6 Ω and scarcely increased to 8.8 and 30.7 Ω after 250, 350 cycles, respectively, demonstrating that the electrode operated very steadily. Also, it's not hard to see from Fig. S4b that the increase in reversible capacity during the range of 150 to 280 cycles is largely to the significant increase in the transformation

reaction at 1.0 ~ 3.0 V potential, which is consistent with the trend of electron transport rate described previously.

To further research the structural and crystal changes of $SnO_2$/C NT electrode after cycling test, a number of testing tools (SEM, TEM and XRD) have been performed. In Figs. S8a, b, the tubular morphology, hollow structure and size of $SnO_2$/C NTs are well maintained, which illustrating the excellent structural stability during lithiation/delithiation process. For comparison, SEM and TEM images of $SnO_2$ NT anode after 200 cycles were shown in Figs. S8c, d. It can be found that the morphology of $SnO_2$ NT was damaged after cycling test. Moreover, Fig. S8e has shown the XRD patterns clearly. The diffraction peaks for $SnO_2$, Sn, Li-Sn alloy, Li$x$C and $Li_2CO_3$ (as products of lithiation reaction and SEI film) are clearly. Then, the $SnO_2$/C NT electrode was reversibly converted to $SnO_2$ and Sn after delithiation process, which further displaying the superior reversible cyclic performance of $SnO_2$/C NT electrodes. Furthermore, comparing the rate performance (Fig. 7) and the cycling performance (Table S3), it can be found that the $SnO_2$/C NT electrodes prepared in this work is superior to those of most other $SnO_2$-based anodes [13, 15, 16, 19, 21, 30, 43, 55-58].

Finally, pouch-type cells were assembled using the $SnO_2$/C NT anode and commercial lithium nickel cobalt manganese oxide (NCM523) cathode. The assembly process is exhibited in Fig. 8a. Figs. 8b, c and Fig. S9 show the rate/cycling performance and galvanostatic charge/discharge curves of the pouch-type cell. As for Fig. 8b, the pouch-type cell exhibits reversible capacities of 674.7, 591.9, 492.1, and 390.6 mhA g$^{-1}$ at 0.1, 0.2, 0.5, and 1.0 A g$^{-1}$, respectively. As for the cycling

performance of the pouch-type cell shown in Fig. 8c, the initial discharge capacity is 705.2 mhA $g^{-1}$ at 0.2 A $g^{-1}$. After 50 cycles at 0.2 A $g^{-1}$, it delivers a high capacity of 474.3 mhA $g^{-1}$. The electrochemical performance of the pouch-type cells further demonstrates the $SnO_2$/C NTs as a promising candidate for LIBs anode.

**4. Conclusion**

In summary, the $SnO_2$/C NTs with highly uniform morphology coated by ultrathin N–doped amorphous carbon film were synthesized successfully using $CuSn(OH)_6$ nanorods as template for the first time. Due to the hollow structure for buffering the volume expansion, N–doped carbon layer for improving conductivity, protecting from pulverization and providing more active sites, which contribute to prominent lithium storage performance. The $SnO_2$/C NT electrode delivers an enhanced capacity of 909.5 mAh $g^{-1}$ at 0.5 A $g^{-1}$ after 200 cycles, and high long-term cyclic stability (551.7 mAh $g^{-1}$ after 500 cycles at 1 A $g^{-1}$) for anode in LIBs. Moreover, it demonstrates impressive rate performance (1069.2 mAh $g^{-1}$ after 280 cycles), which provides a significant improvement over pure $SnO_2$ NT electrode as–prepared, without destroying the original lithium storage mechanism. Therefore, it's worth believing that the synthesis strategy presented in this paper provides an ideal way for the synthesis of transition metal oxides (TMOs)/carbon hollow structure composites by using Sn-based mixed metal hydroxide precursor, and would be prospective in the field of energy storage.

**Reference**

[1] J.B. Goodenough, K.-S. Park, The Li-ion rechargeable battery: a perspective, J. Am. Chem. Soc. 135(4) (2013) 1167-1176.

[2] V. Etacheri, R. Marom, R. Elazari, G. Salitra, D. Aurbach, Challenges in the development of advanced Li-ion batteries: a review, Energy Environ. Sci. 4(9) (2011) 3243.

[3] J. Zheng, M.H. Engelhard, D. Mei, S. Jiao, B.J. Polzin, J.-G. Zhang, W. Xu, Electrolyte additive enabled fast charging and stable cycling lithium metal batteries, Nat. Energy 2(3) (2017).

[4] S. Fang, D. Bresser, S. Passerini, Transition metal oxide anodes for electrochemical energy storage in lithium− and sodium−ion batteries, Advanced Energy Materials 10(1) (2019) 1902485.

[5] W. Ren, Y. Zheng, Z. Cui, Y. Tao, B. Li, W. Wang, Recent progress of functional separators in dendrite inhibition for lithium metal batteries, Energy Storage Mater. 35 (2021) 157-168.

[6] Z. Zheng, P. Li, J. Huang, H. Liu, Y. Zao, Z. Hu, L. Zhang, H. Chen, M.-S. Wang, D.-L. Peng, Q. Zhang, High performance columnar-like $Fe_2O_3$@carbon composite anode via yolk@shell structural design, Journal of Energy Chemistry 41 (2020) 126-134.

[7] J. Wang, C. Wang, M. Zhen, Template-free synthesis of multifunctional $Co_3O_4$ nanotubes as excellent performance electrode materials for superior energy storage, Chemical Engineering Journal 356 (2019) 1-10.

[8] D. Narsimulu, G. Nagaraju, S. Chandra Sekhar, B. Ramulu, J. Su Yu, Three-dimensional porous $SnO_2$/carbon cloth electrodes for high-performance lithium- and sodium-ion batteries, Applied Surface Science 538 (2021) 148033.

[9] Y.-N. Sun, M. Goktas, L. Zhao, P. Adelhelm, B.-H. Han, Ultrafine $SnO_2$ nanoparticles anchored on N, P-doped porous carbon as anodes for high performance lithium-ion and sodium-ion batteries, J. Colloid Interface Sci. 572 (2020) 122-132.

[10] M. Agostini, S. Brutti, J. Hassoun, High voltage Li-ion battery using exfoliated graphite/graphene nanosheets Anode, ACS Appl. Mater. Interfaces 8(17) (2016) 10850-10857.

[11] Y. Hong, W. Mao, Q. Hu, S. Chang, D. Li, J. Zhang, G. Liu, G. Ai, Nitrogen-doped carbon coated $SnO_2$ nanoparticles embedded in a hierarchical porous carbon framework for high-performance lithium-ion battery anodes, J. Power Sources 428 (2019) 44-52.

[12] L. Ao, C. Wu, X. Wang, Y. Xu, K. Jiang, L. Shang, Y. Li, J. Zhang, Z. Hu, J. Chu, Superior and reversible lithium storage of $SnO_2$/graphene composites by silicon doping and carbon sealing, ACS Appl. Mater. Interfaces 12(18) (2020) 20824-20837.

[13] B. Han, W. Zhang, D. Gao, C. Zhou, K. Xia, Q. Gao, J. Wu, Encapsulating tin oxide nanoparticles into holey carbon nanotubes by melt infiltration for superior lithium and sodium ion storage, J. Power Sources 449 (2020) 227564.

[14] B. Cao, Z. Liu, C. Xu, J. Huang, H. Fang, Y. Chen, High-rate-induced capacity evolution of mesoporous C@$SnO_2$@C hollow nanospheres for ultra-long cycle lithium-ion batteries, J. Power Sources 414 (2019) 233-241.

[15] Q. Wu, Q. Shao, Q. Li, Q. Duan, Y. Li, H.-g. Wang, Dual carbon-confined $SnO_2$

hollow nanospheres enabling high performance for the reversible storage of alkali metal ions, ACS Appl. Mater. Interfaces 10(18) (2018) 15642-15651.

[16] N. Wu, W. Du, X. Gao, L. Zhao, G. Liu, X. Liu, H. Wu, Y.-B. He, Hollow $SnO_2$ nanospheres with oxygen vacancies entrapped by a N-doped graphene network as robust anode materials for lithium-ion batteries, Nanoscale 10(24) (2018) 11460-11466.

[17] S. Gao, N. Wang, S. Li, D. Li, Z. Cui, G. Yue, J. Liu, X. Zhao, L. Jiang, Y. Zhao, A Multi−wall Sn/$SnO_2$@carbon hollow nanofiber anode material for high−rate and long−life lithium−ion batteries, Angew. Chem. Int. Ed. 59(6) (2020) 2465-2472.

[18] O.H. Kwon, J.H. Oh, B. Gu, M.S. Jo, S.H. Oh, Y.C. Kang, J.K. Kim, S.M. Jeong, J.S. Cho, Porous $SnO_2$/C nanofiber anodes and $LiFePO_4$/C nanofiber cathodes with a wrinkle structure for stretchable lithium polymer batteries with high electrochemical performance, Adv. Sci. 7(17) (2020) 2001358.

[19] S. Kong, J. Xu, G. Lin, S. Zhang, W. Dong, J. Wang, F. Huang, A rationally designed 3D interconnected porous tin dioxide cube with reserved space for volume expansion as an advanced anode of lithium-ion batteries, Chem. Commun. 56(71) (2020) 10289-10292.

[20] Q. Tian, Y. Chen, W. Zhang, J. Chen, L. Yang, Self-sacrificing template strategy to facilely prepare well-defined $SnO_2$@C quasi-hollow nanocubes for lithium-ion battery anode, Applied Surface Science 507 (2020) 145189.

[21] Q. Tian, F. Zhang, W. Zhang, L. Yang, Non-smooth carbon coating porous $SnO_2$ quasi-nanocubes towards high lithium storage, Electrochimica Acta 307 (2019)

393-402.

[22] J. Yan, P. Xu, S. Chen, G. Wang, F. Zhang, W. Zhao, Z. Zhang, Z. Deng, M. Xu, J. Yun, Y. Zhang, Construction of highly ordered ZnO microrod@SnO$_2$ nanowire heterojunction hybrid with a test-tube brush-like structure for high performance lithium-ion batteries: experimental and theoretical study, Electrochimica Acta 330 (2020) 135312.

[23] B. Song, P. Loya, L. Shen, C. Sui, L. He, H. Guo, W. Guo, M.-T.F. Rodrigues, P. Dong, C. Wang, X. He, P.M. Ajayan, J. Lou, Quantitative in situ fracture testing of tin oxide nanowires for lithium ion battery applications, Nano Energy 53 (2018) 277-285.

[24] L. Zhang, K. Zhao, R. Yu, M. Yan, W. Xu, Y. Dong, W. Ren, X. Xu, C. Tang, L. Mai, Phosphorus enhanced intermolecular interactions of SnO$_2$ and graphene as an ultrastable lithium battery anode, Small 13(20) (2017) 1603973.

[25] M. Liu, H. Fan, O. Zhuo, J. Chen, Q. Wu, L. Yang, L. Peng, X. Wang, R. Che, Z. Hu, A general strategy to construct yolk-shelled metal oxides inside carbon nanocages for high-stable lithium-ion battery anodes, Nano Energy 68 (2020) 104368.

[26] Y. Pang, J. Wang, J. Yang, F. Fang, D. Sun, S. Zheng, Fully reversible lithium storage of tin oxide enabled by self-doping and partial amorphization, Nanoscale 11(27) (2019) 12915-12923.

[27] S. Fu, Q. Wu, S. He, S. Tong, X. Yang, Y. Meng, M. Wu, Ultrafine SnO$_2$ nanocrystals self-anchored in carbon for stable lithium storage, ChemElectroChem

5(17) (2018) 2341-2347.

[28] W. Li, Z. Chen, J. Hou, T. Xu, D. Liu, S. Leng, H. Guo, C. Chen, J. Yang, M. Wu, $SnO_2$ nano-crystals anchored on N-doped porous carbon with enhanced lithium storage properties, Applied Surface Science 515 (2020) 145902.

[29] F. Li, G. Luo, W. Chen, Y. Chen, Y. Fang, M. Zheng, X. Yu, Rational design and controllable synthesis of multishelled $Fe_2O_3@SnO_2@C$ nanotubes as advanced anode material for lithium-/sodium-ion batteries, ACS Appl. Mater. Interfaces 11(40) (2019) 36949-36959.

[30] Q. Tian, Y. Chen, F. Chen, J. Chen, L. Yang, Walnut core-like hollow carbon micro/nanospheres supported $SnO_x@C$ composite for high performance lithium-ion battery anode, J. Colloid Interface Sci. 554 (2019) 424-432.

[31] X.W. Lou, Y. Wang, C. Yuan, J.Y. Lee, L.A. Archer, Template-free synthesis of $SnO_2$ hollow nanostructures with high lithium storage capacity, Adv. Mater. 18(17) (2006) 2325-2329.

[32] Y. Liu, X. Li, Y. Wang, X. Li, P. Cheng, Y. Zhao, F. Dang, Y. Zhang, Hydrothermal synthesis of $Au@SnO_2$ hierarchical hollow microspheres for ethanol detection, Sensors and Actuators B: Chemical 319 (2020) 128299.

[33] Y. Xu, L. Zheng, C. Yang, X. Liu, J. Zhang, Highly sensitive and selective electronic sensor based on Co catalyzed $SnO_2$ nanospheres for acetone detection, Sensors and Actuators B: Chemical 304 (2020) 127237.

[34] Q. Tian, F. Chen, Y. Liu, K. Chen, L. Yang, Stabilizing the nanostructure of $SnO_2$ anode by constructing heterogeneous yolk@shell hollow composite, Applied

Surface Science 493 (2019) 838-846.

[35] S.-W. Park, S.-Y. Jeong, J.-W. Yoon, J.-H. Lee, General strategy for designing highly selective gas-sensing nanoreactors: Morphological control of $SnO_2$ hollow spheres and configurational tuning of Au catalysts, ACS Appl. Mater. Interfaces 12(46) (2020) 51607-51615.

[36] J. Lu, L. Lan, X.T. Liu, N. Wang, X. Fan, Plasmonic Au nanoparticles supported on both sides of $TiO_2$ hollow spheres for maximising photocatalytic activity under visible light, Front. Chem. Sci. Eng. 13(4) (2019) 665-671.

[37] B. Ren, J. Lu, Y. Wang, X. Gu, B.B. Xu, Y. Fu, K. Luo, M. Bayati, T.X. Liu, Half-sphere shell supported Pt catalyst for electrochemical methanol oxidation, J. Electrochem. Soc. 167(8) (2020) 084510.

[38] J.R. Huang, X.J. Xu, C.P. Gu, S.Y. Yao, Y.F. Sun, J.H. Liu, Large-scale selective preparation of porous $SnO_2$ 3D architectures and their gas-sensing property, CrystEngComm 14(9) (2012) 3283.

[39] S. Huang, Z. Li, B. Wang, J. Zhang, Z. Peng, R. Qi, J. Wang, Y. Zhao, N-doping and defective nanographitic domain coupled hard carbon nanoshells for high performance lithium/sodium storage, Adv. Funct. Mater. 28(10) (2018) 1706294.

[40] A.Y. Kim, R.E.A. Ardhi, G. Liu, J.Y. Kim, H.-J. Shin, D. Byun, J.K. Lee, Hierarchical hollow dual Core–Shell carbon nanowall-encapsulated p–n $SnO/SnO_2$ heterostructured anode for high-performance lithium-ion-based energy storage, Carbon 153 (2019) 62-72.

[41] K.H. Lim, H. Kweon, H. Kim, Polydopamine-derived nitrogen-doped graphitic

carbon for a bifunctional oxygen electrode in a non-aqueous Li-O$_2$ battery, J. Electrochem. Soc., 164 (2017) A1595-A1600.

[42] H.Q. Wang, Q.C. Pan, Q. Wu, X.H. Zhang, Y.G. Huang, A. Lushington, Q.Y. Li, X.L. Sun, Ultrasmall MoS$_2$ embedded in carbon nanosheets-coated Sn/SnO$_x$ as anode material for high-rate and long life Li-ion batteries, J. Mater. Chem. A, 5 (2017) 4576-4582.

[43] S.M. Jung, D.W. Kim, H.Y. Jung, Unconventional capacity increase kinetics of a chemically engineered SnO$_2$ aerogel anode for long-term stable lithium-ion batteries, J. Mater. Chem. A 8(17) (2020) 8244-8254.

[44] J. Kong, W.A. Yee, L. Yang, Y. Wei, S.L. Phua, H.G. Ong, J.M. Ang, X. Li, X. Lu, Highly electrically conductive layered carbon derived from polydopamine and its functions in SnO$_2$-based lithium ion battery anodes, Chem. Commun. 48(83) (2012) 10316.

[45] X. Zhao, X. Liu, C. Yi, J. Li, Y. Su, M. Guo, Palladium nanoparticles embedded in yolk–shell N-doped carbon nanosphere@void@SnO$_2$ composite nanoparticles for the photocatalytic reduction of 4-nitrophenol, ACS Appl. Nano Mater. 3(7) (2020) 6574-6583.

[46] L.S. Cui, C.L. Tan, G.H. Yang, Y. Li, Q.C. Pan, M. Zhang, Z.L. Chen, F.H. Zheng, H.Q. Wang, Q.Y. Li, Constructing an interface synergistic effect from a SnS/MoS$_2$ heterojunction decorating N, S co-doped carbon nanosheets with enhanced sodium ion storage performance, J. Mater. Chem. A, 8 (2020) 22593-22600.

[47] F.F. Li, G.W. Wang, D. Zheng, X.X. Zhang, C.J. Abegglen, H.N. Qu, D.Y. Qu,

Controlled prelithiation of $SnO_2$/C nanocomposite anodes for building full lithium-ion batteries, ACS Appl. Mater. Interfaces 12 (17) (2020) 19423-19430.

[48] G.W. Wang, F.F. Li, D. Liu, D. Zheng, Y. Luo, D.Y. Qu, T.Y. Ding, D.Y. Qu, Chemical prelithiation of negative electrodes in ambient air for advanced lithium-ion batteries, ACS Appl. Mater. Interfaces, 11 (2019) 8699-8703.

[49] Y. Qian, S. Jiang, Y. Li, Z. Yi, J. Zhou, J. Tian, N. Lin, Y.T Qian, Understanding mesopore volume-enhanced extra-capacity: Optimizing mesoporous carbon for high-rate and long-life potassium-storage, Energy Storage Mater., 29 (2020) 341-349.

[50] Y.G. Huang, Q.C. Pan, H.Q. Wang, C. Ji, X.M. Wu, Z.Q. He, Q.Y. Li, Preparation of a $Sn@SnO_2@C@MoS_2$ composite as a high-performance anode material for lithium-ion batteries, J. Mater. Chem. A, 4 (2016) 7185-7189.

[51] W. Dong, J. Xu, C. Wang, Y. Lu, X. Liu, X. Wang, X. Yuan, Z. Wang, T. Lin, M. Sui, I.W. Chen, F. Huang, A robust and conductive black tin oxide nanostructure makes efficient lithium-ion batteries possible, Adv. Mater. 29(24) (2017) 1700136.

[52] L. Zhang, H.B. Wu, B. Liu, X.W. Lou, Formation of porous $SnO_2$ microboxes via selective leaching for highly reversible lithium storage, Energy Environ. Sci. 7(3) (2014) 1013.

[53] X. Zhou, L. Yu, X.W.D. Lou, Formation of uniform N-doped carbon-coated $SnO_2$ submicroboxes with enhanced lithium storage properties, Advanced Energy Materials 6(14) (2016) 1600451.

[54] Y. Chen, T. Wu, W. Chen, W. Zhang, L. Zhang, Z. Zhu, M. Shao, B. Zheng, S. Li,

W. Zhang, W.-B. Pei, J. Wu, F. Huo, $Co_3O_4$ nanoparticles embedded in nitrogen-doped graphitic carbon fibers as a free-standing electrode for promotion of lithium ion storage with capacitive contribution, Chem. Commun. 56(43) (2020) 5767-5770.

[55] Q. Tan, Z. Kong, X. Chen, L. Zhang, X. Hu, M. Mu, H. Sun, X. Shao, X. Guan, M. Gao, B. Xu, Synthesis of $SnO_2$/graphene composite anode materials for lithium-ion batteries, Applied Surface Science 485 (2019) 314-322.

[56] M. Sahoo, S. Ramaprabhu, One-pot environment-friendly synthesis of boron doped graphene-$SnO_2$ for anodic performance in Li ion battery, Carbon 127 (2018) 627-635.

[57] H. Mao, L. Shi, S. Song, C. Xiao, J. Liang, B. Dong, S. Ding, N-Doped hollow carbon nanosheet supported $SnO_2$ nanoparticles, Inorg. Chem. Front. 4(10) (2017) 1742-1747.

[58] D. Yang, H. Ren, D. Wu, W. Zhang, X. Lou, D. Wang, K. Cao, Z. Gao, F. Xu, K. Jiang, Bi-functional nitrogen-doped carbon protective layer on three-dimensional RGO/$SnO_2$ composites with enhanced electron transport and structural stability for high-performance lithium-ion batteries, J. Colloid Interface Sci. 542 (2019) 81-90.

**Figures**
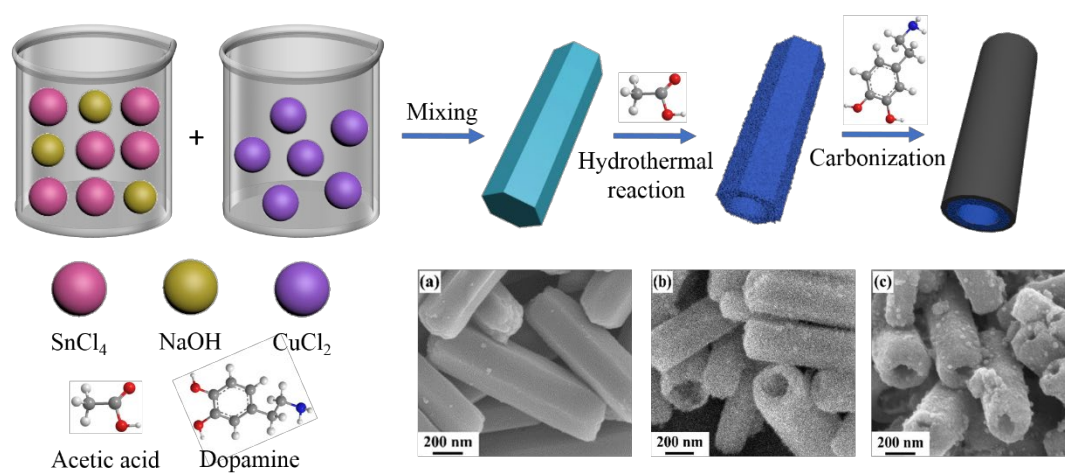


**Scheme 1** (a) Schematic illustration of preparation process of $SnO_2$/C NTs with SEM images of (b) $CuSn(OH)_6$ nanorods, (c) $SnO_2$ NTs and (d) $SnO_2$/C NTs.
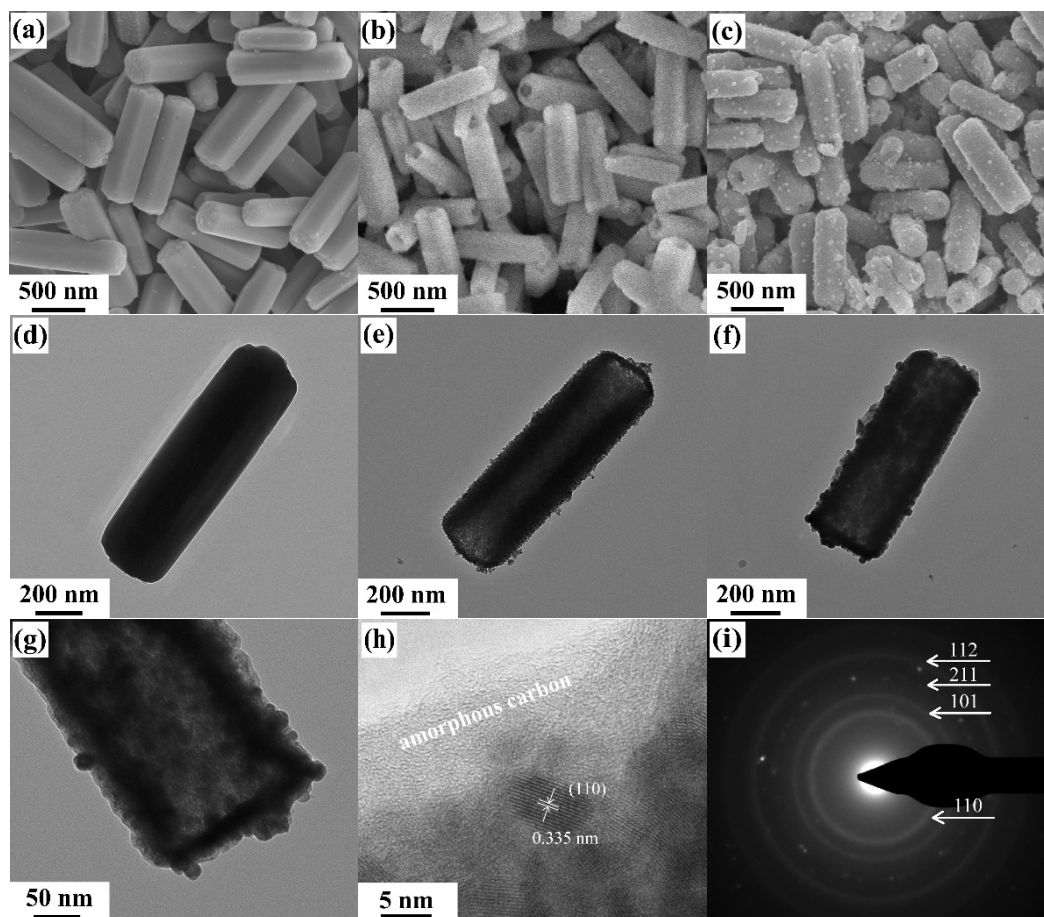
**Fig. 1** (a-c) SEM and (d-f) TEM images of CuSn(OH)$_6$, SnO$_2$ NTs and SnO$_2$/C NTs. (g) high magnification TEM image of SnO$_2$/C NTs, (h) HRTEM image and (i) SAED pattern of SnO$_2$/C NTs.
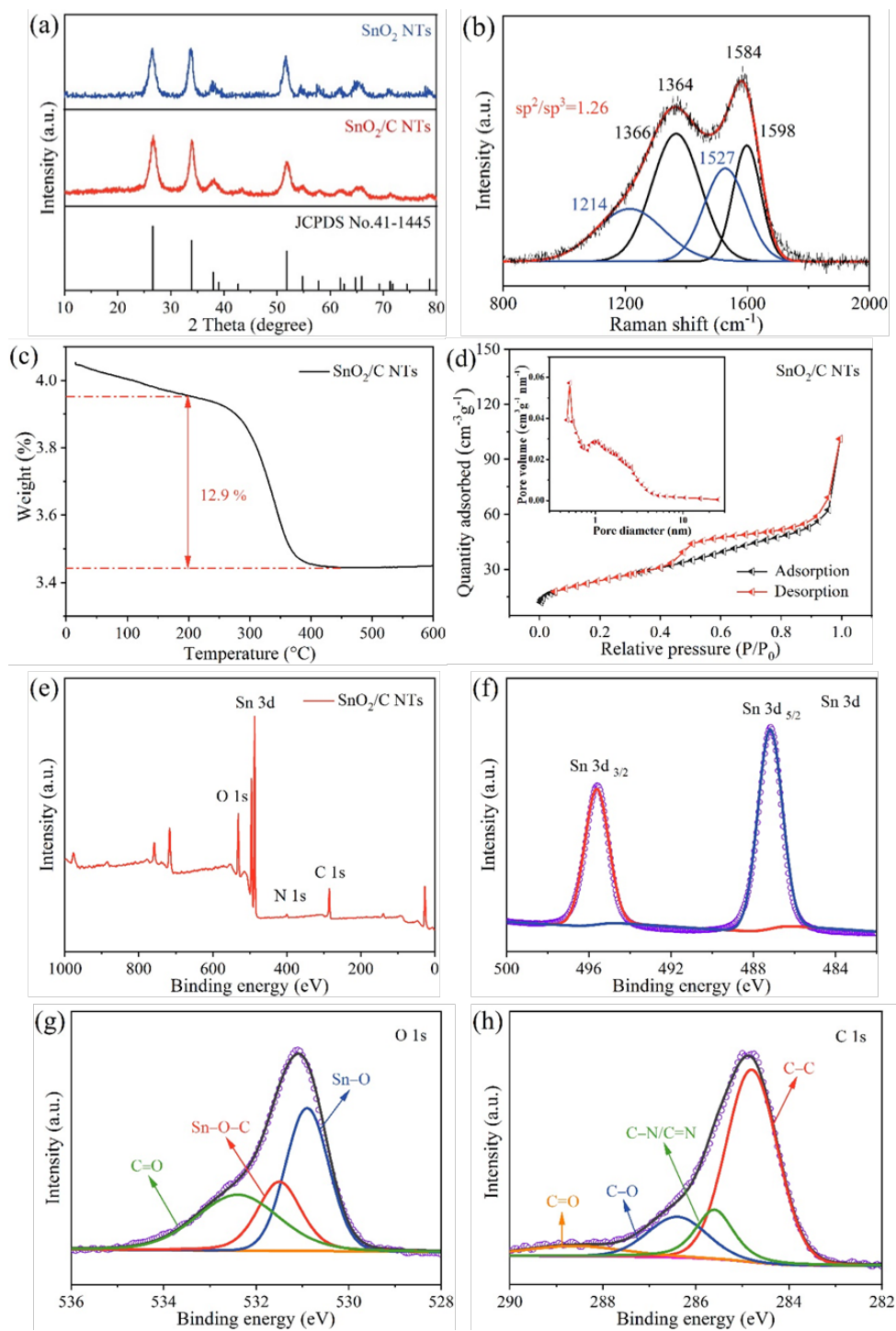
**Fig. 2** (a) XRD patterns of SnO$_2$ NTs and SnO$_2$/C NTs, (b) Raman spectrum of SnO$_2$/C,

(c) TGA curve and (d) N$_2$ adsorption/desorption isotherms of SnO$_2$/C, the inset shows

the corresponding pore size distribution curve. (e) XPS survey spectrum and (f–h) high

resolution (f) Sn 3d, (g) O 1s, and (h) C 1s XPS spectra of SnO$_2$/C.
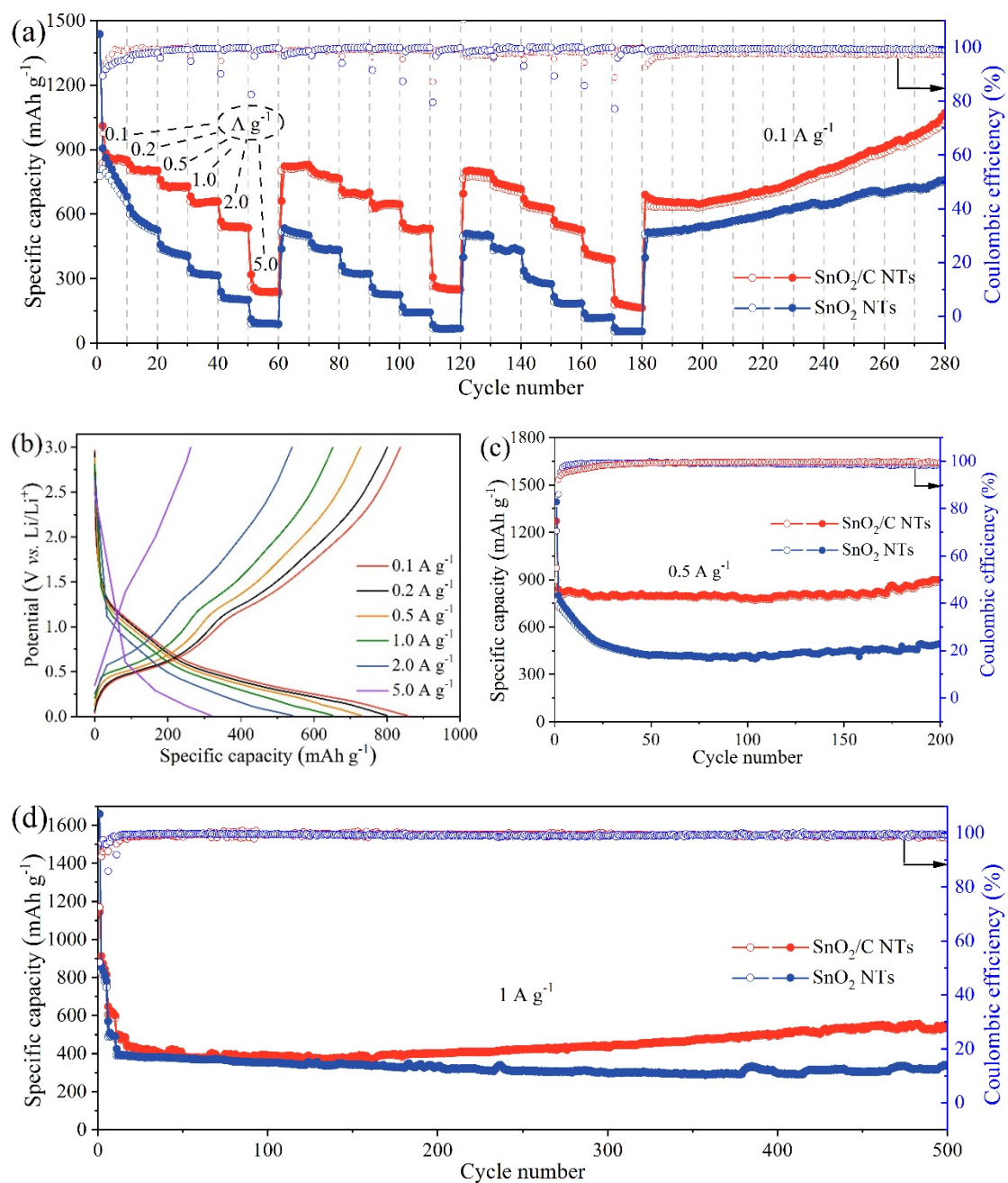
**Fig. 3** (a) Rate performance of $SnO_2$/C NT and $SnO_2$ NT electrodes at various current densities. (b) Galvanostatic charge/discharge curves of $SnO_2$/C NTs at increasing current density from 0.1 to 5.0 A $g^{-1}$. The curves are selected from the middle circle of each rate in the first round. Cycling performances and Coulombic efficiency of $SnO_2$/C NT and $SnO_2$ NT electrodes at (c) 0.5 A $g^{-1}$, and (d) 1.0 A $g^{-1}$.
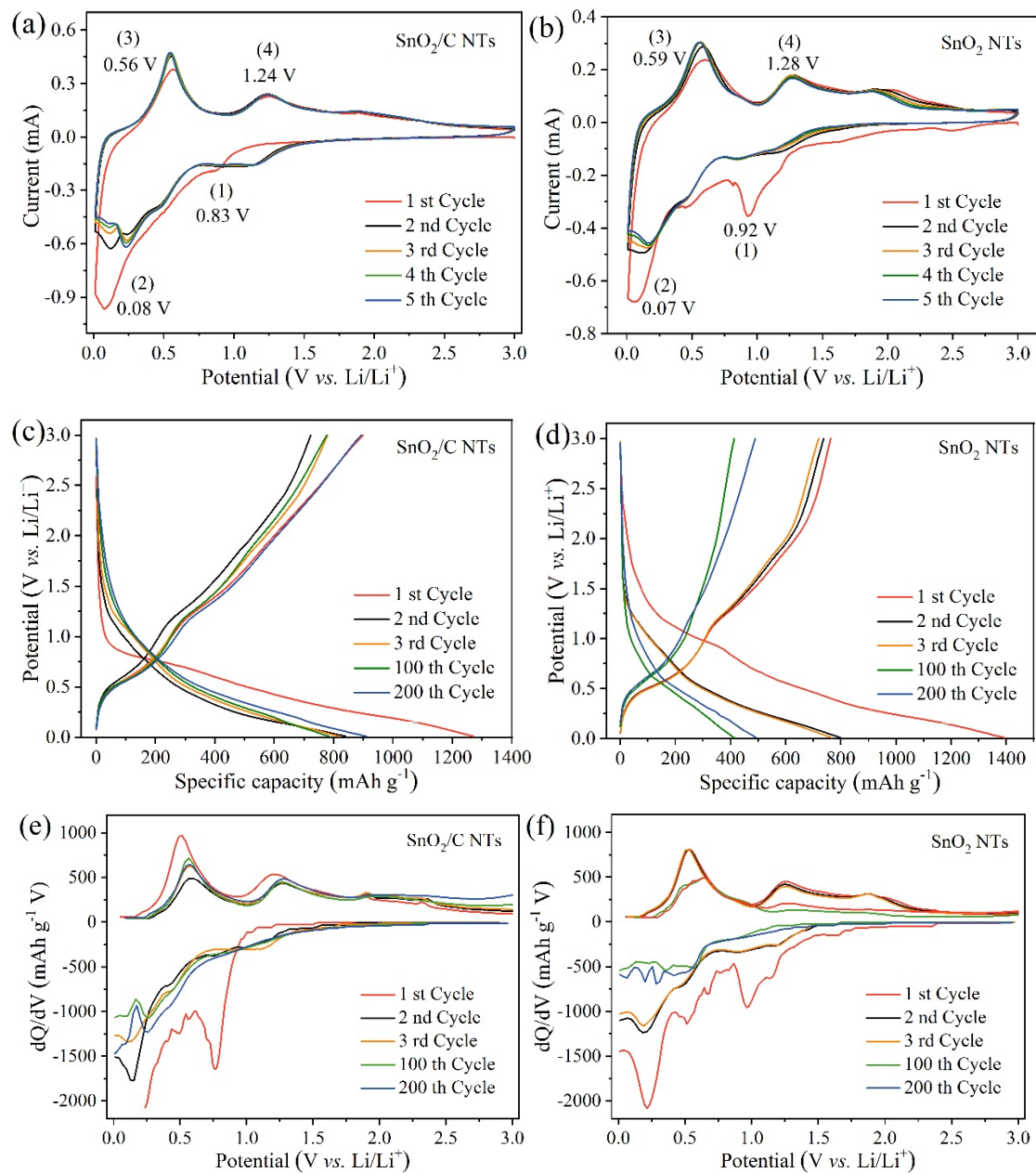
**Fig. 4** CV curves of (a) SnO₂/C NT electrode and (b) SnO₂ NT electrode at a scan rate

of 0.1 mV s⁻¹ in range of 0.01−3.0 V *vs.* Li/Li⁺. Galvanostatic charge/discharge curves

of (c) SnO₂/C NT electrode and (d) SnO₂ NT electrode for the 1st, 2nd, 3rd, 100th, and

200th cycles at 0.5 A g⁻¹. The differential charge/discharge capacity curves of (e)

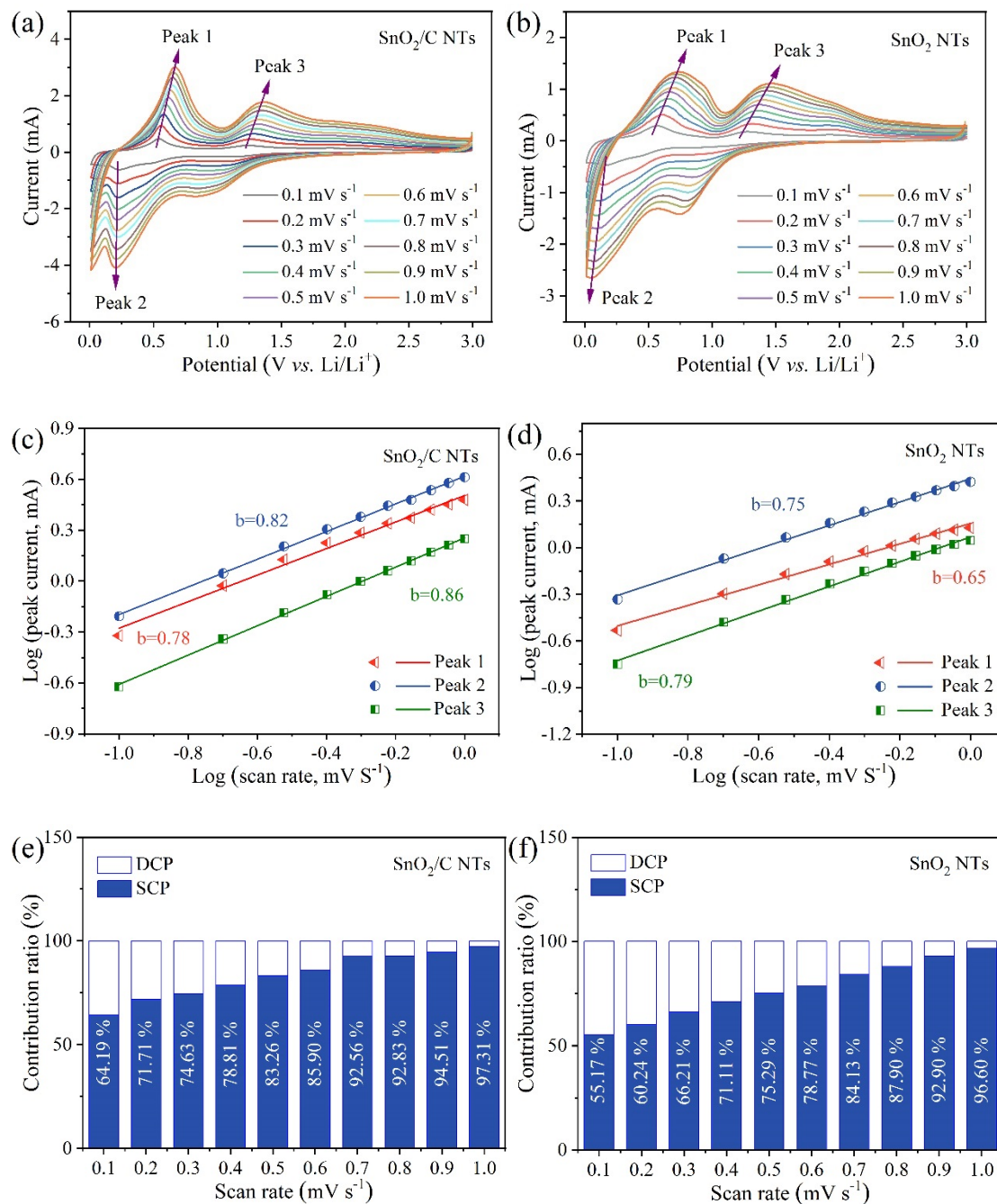SnO₂/C NTs and (f) SnO₂ NTs at the 1st, 2nd, 3rd, 100th, and 200th cycles at 0.5 A g⁻

¹.

**Fig. 5** CV curves of (a) SnO$_2$/C NT electrode and (b) SnO$_2$ NT electrode at various scan rates. The fitted specific anodic/cathodic peak current for determining *b* value of (c) SnO$_2$/C NT electrode and (d) SnO$_2$ NT electrode. Column diagrams of capacitive ratio for (e) SnO$_2$/C NT electrode and (f) SnO$_2$ NT electrode at various scan rates.
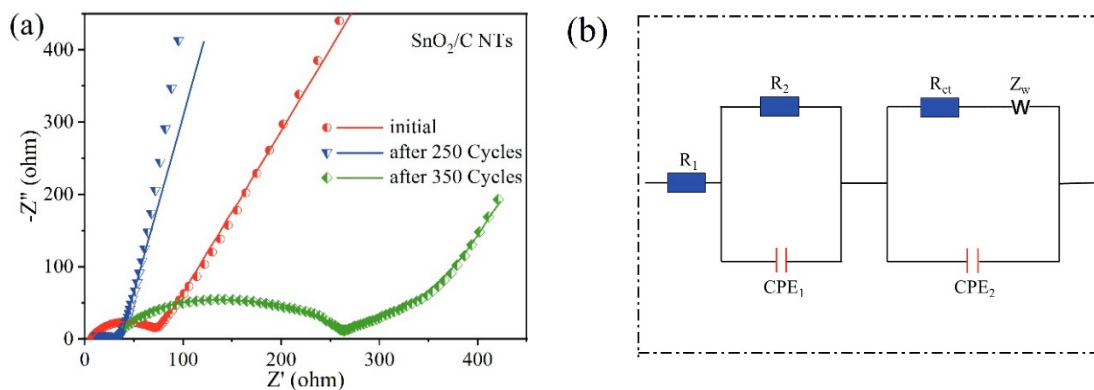
**Fig. 6** (a) Electrochemical impedance spectra (symbol) and the fitting curves (line) of SnO$_2$/C NT electrode for initial and after 250 and 350 cycles. (b) Equivalent circuit used in EIS.
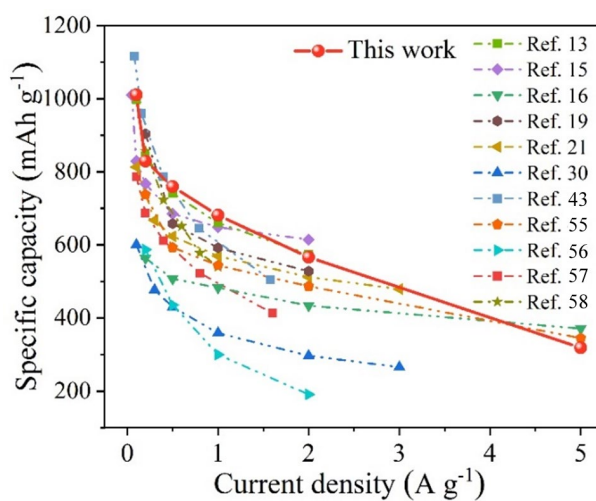


**Fig. 7** Rate performance comparison of SnO$_2$/C NT electrode and previously reported SnO$_2$-based anode materials.
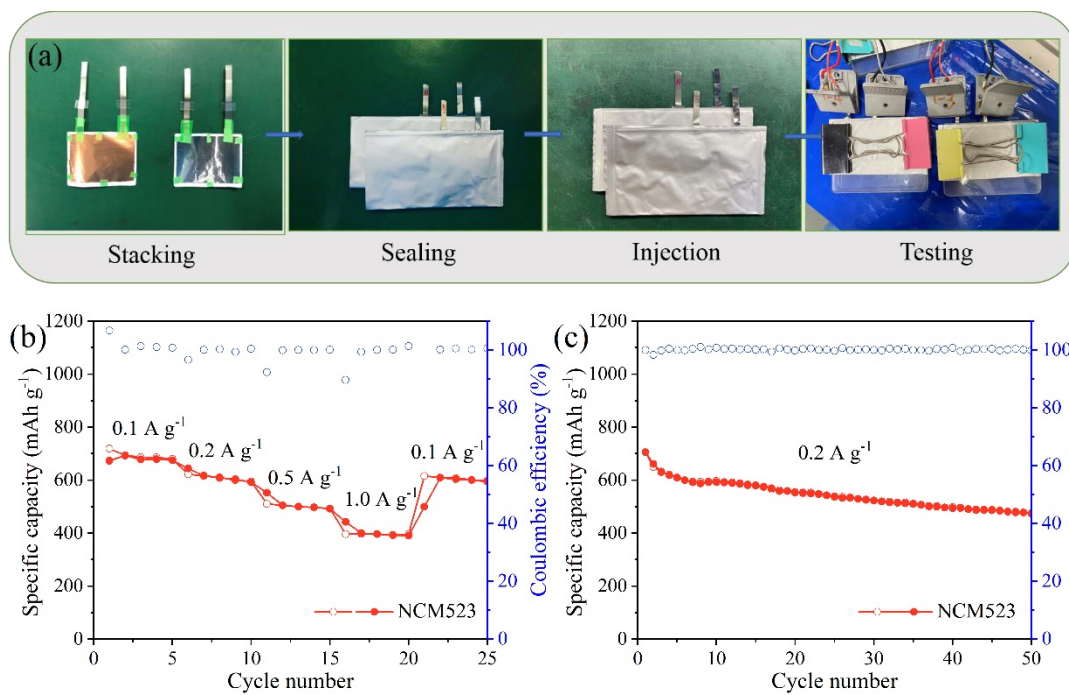
**Fig. 8** (a) Illustration of pouch-type cell assembly. Electrochemical performance of pouch-type cells with SnO$_2$/C NT anode and NCM523 cathode in the potential window of 1.5 to 4.3 V: (b) rate performance and (c) cycling performance at 0.2 A g$^{-1}$.